

Published in final edited form as:

J Comput Neurosci. 2013 October ; 35(2): 231–241. doi:10.1007/s10827-013-0450-z.

A molecular level prototype for mechanoelectrical transducer in mammalian hair cells

Jinkyong Park and

Department of Mathematics Michigan State University, MI 48824, USA

Guo-Wei Wei

Department of Mathematics Michigan State University, MI 48824, USA

Department of Biochemistry and Molecular Biology Michigan State University, MI 48824, USA

Guo-Wei Wei: wei@math.msu.edu

Abstract

The mechanoelectrical transducer (MET) is a crucial component of mammalian auditory system. The gating mechanism of the MET channel remains a puzzling issue, though there are many speculations, due to the lack of essential molecular building blocks. To understand the working principle of mammalian MET, we propose a molecular level prototype which constitutes a charged blocker, a realistic ion channel and its surrounding membrane. To validate the proposed prototype, we make use of a well-established ion channel theory, the Poisson-Nernst-Planck equations, for three-dimensional (3D) numerical simulations. A wide variety of model parameters, including bulk ion concentration, applied external voltage, blocker charge and blocker displacement, are explored to understand the basic function of the proposed MET prototype. We show that our prototype prediction of channel open probability in response to blocker relative displacement is in a remarkable accordance with experimental observation of rat cochlea outer hair cells. Our results appear to suggest that tip links which connect hair bundles gate MET channels.

Keywords

Mechanoelectrical transducer; Gating mechanism; Poisson-Nernst-Planck model; Ion channel

1 Introduction

The sense of hearing, one of the five major senses, is important for human to communicate with and perceive the world. The human sensory system for hearing is the auditory system that consists of the outer, middle and inner ears (Borisjuk, 2005). This system detects a wide range of sounds, amplifies waves and converts them into electrical signals so that the brain can analyze and interpret auditory information (Borisjuk, 2005). In detail, sound waves in the air go through the external canal of the outer ear and are transformed into pressure waves by the middle ear. The pressure waves vibrate the basilar membrane in the cochlea of the inner ear, which regulates the movement of hair bundles (Peng et al, 2011). It is widely believed that the deflection of hair bundles opens mechanoelectrical transducer (MET) channels to generate electrical signals acceptable by the brain (Borisjuk, 2005; Schwander et al, 2010; Peng et al, 2011).

For many mammals, the organ of Corti, a part of the cochlea, contains one row of inner hair cells (IHCs) and three rows of outer hair cells (OHCs) with different functions and shapes. The IHC is a transducer which takes acoustic information to afferent neurons, while OHC is a cochlea amplifier which manages vibrations of the basilar membrane (Fettiplace and Hackney, 2006). In fact, the mechanically sensitive hair bundles are located at the apical surface of hair cells and each of them is composed of several actin-filled microvilli, also named stereocilia (Peng et al, 2011). The stereocilia are arranged in rows of decreasing height and are tightly connected to each other by extracellular linkages including tip links and top-connectors (Schwander et al, 2010). The gating mechanism of the MET channel is one of the most interesting research topics. It is speculated that the tip link, which extends from the tip of a stereocilium to the side of the next taller one, has been thought to gate the MET channel directly or indirectly (Schwander et al, 2010; Kazmierczak and Müller, 2012).

The MET channel is a nonselective cation channel with a considerably high permeability of Ca^{2+} (Fettiplace, 2009). The permeability of Ca^{2+} has been used to identify the localization of the MET channels (Denk et al, 1995; Jaramillo and Hudspeth, 1991). Especially, Beurg *et al.* have shown that MET channels are located at the bottom of the tip links as indicated by fast confocal calcium-imaging (Beurg et al, 2009). The molecular structure of the MET channel is still obscure, partly because of few channels per hair cell and few hair cells per organ (Peng et al, 2011). Although several candidates were suggested in the literature, none of them was perfectly matched with the MET channel from biophysical perspective (Fettiplace, 2009). Ricci *et al.* showed that the conductance of hair cells was tono-topically changed, which implies that the MET channel might be composed of several subunits (Ricci et al, 2003). Farris and his colleagues measured the pore size and channel length using various antagonists of the candidate channel classes (Farris et al, 2004). More intrinsic characteristics of the MET channel are yet to be discovered in order to construct its molecular identity.

The biophysical principles underlying the mechanotransduction process in hair cells have been intensively investigated in the past few decades. It is postulated that defection of a hair bundle toward the longest stereocilia, namely positive deflection, leads to open the MET channels at the lower end of the tip links (Kazmierczak and Müller, 2012). The tip link and an elusive elastic element, namely gating spring, are believed to unfasten the channel. Then Ca^{2+} enters through the channel and contributes to fast adaptation by binding to a molecule inside or near the channel. Finally, slow adaptation is accomplished by a myosin motor at the upper end of the tip link in two steps. First, sliding down of the motor along the stereocilia results in channel closure, and then its climbing toward the tip leads to restore tension (Ricci et al, 2006; Schwander et al, 2010; Kazmierczak and Müller, 2012). Despite much advance, the molecular detail of the mechanotransduction machinery has proved to be elusive. Particularly, there is no direct structural confirmation for the molecular building blocks of MET channels.

Ion channels have received a great attention from physicists, biochemists and biologists. Ion channels are membrane proteins with a pore which govern ion permeability through the membrane. The major roles of ion channels are to alter membrane potentials, to control electrolyte movements for cell volume regulation and polarized transport of salt, and to generate electrical signals which are utilized to regulate hormone secretion, neurotransmitter release and muscle contraction (Hacker et al, 2009). Ion channels can be mainly classified by ion selectivity and gating mechanism. Most channels are very selective in allowing permeation of certain ions although there are exceptions, i.e., nonselective cation channels (Hacker et al, 2009). Potassium, sodium, calcium and chloride are four principal ions in mammalian sensory systems. Indeed, they are of crucial importance for the electrical excitability (Hacker et al, 2009). In the view of the gating mechanism, ion channels are

generally classified as voltage-gated or ligand-gated (Hacker et al, 2009). Voltage-gated channels are opened or closed by transmembrane voltage; on the other hand, ligand-gated channels are done by conformational changes. Nonetheless, ion channels can also be gated by photonic, thermal and mechanical means.

In 1952, Hodgkin and Huxley modeled the action potential in squid giant axons by analyzing electrical movements of Na^+ and K^+ through the ion channels (Hodgkin and Huxley, 1952). Since then, there has been tremendous progress in developing experimental techniques and theoretical tools to investigate structure, function, dynamics and transport of ion channels in electrophysiology, biochemistry, molecular biology, computational chemistry and bioinformatics (Jordan, 2005). Electron microscopy, nuclear magnetic resonance spectroscopy and X-ray crystallography have been established to reveal structural information of ion channels (Jordan, 2005). Furthermore, several powerful theoretical tools, such as molecular dynamics (MD), Brownian dynamics (BD), Poisson-Nernst-Planck (PNP) model, Poisson-Boltzmann-Nernst-Planck (PBNP) model and variational multiscale models, have been advanced over years to examine ion channels (Chen and Eisenberg, 1993; Hollerbach et al, 2001; Roux et al, 2004; Jordan, 2005; Coalson and Kurnikova, 2005; Lu et al, 2007; Jung et al, 2009; Zheng and Wei, 2011; Chen and Wei, 2012; Wei et al, 2012). The MD provides a detailed molecular-level approach by describing the dynamical motions of all the atoms in the system via the Newton's second law of motion (Roux et al, 2004; Jordan, 2005). The BD also describes the motion of every ion in the molecular level, but it considers the solvent as a dielectric continuum (Roux et al, 2004; Jordan, 2005). The PNP model, an electrodiffusion approach, treats both ions and solvent as continuous entities and describes membrane protein in atomic detail (Chen and Eisenberg, 1993; Eisenberg et al, 2010; Coalson and Kurnikova, 2005). The PBNP model simplifies the PNP calculation for multiple ions (Lu et al, 2007; Zheng and Wei, 2011). Variational formulations are proposed to derive a variety of multiscale models for charge transport (Wei et al, 2012).

The purpose of the present work is to explore the gating mechanism of the MET channel in mammalian hair cells. We construct a molecular level prototype to probe into the mechanical gating principle of the MET channel. Our model consists of a realistic ion channel, a membrane and an additional charged lip. Our theoretical analysis has been carried out with the PNP model which is able to provide channel currents under various experimental conditions, such as bulk ion concentration, applied voltage, lip charge and lip position. In particular, we examine the response of channel current according to lip displacement. Our results are compared with experimental data of rat hair bundle displacement and current relation given by Kennedy *et al.* (Kennedy et al, 2005).

The rest of this paper is organized as follows. In Section 2, our molecular level prototype for the MET channel is presented, followed by a description of the PNP model and its computational algorithm. Since the molecular structure of the MET channel is unknown, an alternative channel is needed. We use the Gramicidin A (GA) ion channel (PDB ID: 1MAG) for the following reasons. First, the structure of GA is simple so that a blocker can be added with 100% confidence in the blocker's geometry. Many other channels have additional domains which may cause unwanted complication in the result interpretation. Additionally, the GA is one of the most studied realistic channels and its behavior is well-known (Zheng and Wei, 2011; Chen and Wei, 2012; Wei et al, 2012). Consequently, the change in behavior can be easily attributed to the blocker effect. A particle-like lip with an adjustable charge is mounted at the mouth region of the GA channel to enable the mechanoelectrical gating of the channel. The PNP theory is implemented via the second-order PNP solver recently developed in our lab (Zheng et al, 2011) to compute electrostatic potential and current in the prototype channel. Section 3 is devoted to the numerical study of our prototype for the MET channel. We validate our model by analyzing the electrostatic potential and channel current

under a variety of channel conditions. Our computational results including electrostatic potential profiles and open probability distributions are compared with experimental data in the literature. This paper ends with a conclusion.

2 Model and algorithm

2.1 Geometry of the MET prototype

Howard and Hudspeth (Howard and Hudspeth, 1988) proposed the original gating spring model, in which the elastic component, the so-called gating spring, regulates opening and closing of the transducer channels. Deflection of a hair bundle toward the tallest row of stereocilia increases the tension of the spring attached to the hypothetical channel gate, which opens the channels. It was assumed that the tip link acted as a gating spring. However, recent research findings suggest that the tip link may be too stiff to express a spring effect and thus the elastic filament may be located at the bottom of the channel (Gillespie and Müller, 2009; Kazmierczak et al, 2007; Schwander et al, 2010). It is still mysterious how the deflection of a hair bundle gives rise to opening the MET channels. Several possibilities are suggested, but none of them is conclusive owing to the lack of molecular level structural information for the MET channel and insufficient experimental evidence. Moreover, the channel opening may involve not only a conformational change but also a complicated molecular interplay (Ricci et al, 2006; Peng et al, 2011).

In this work, we construct a molecular level prototype to simulate the MET channel gating process. The GA channel is employed to represent the channel structure. A positively charged ion of radius 1.5 Å, called as a “blocker”, is placed at the mouth region of the channel to behave as a lip, see Fig. 1. Since the GA channel is a cation channel, it can be effectively blocked by an additional cation with a pertinent charge.

The structural data of the GA channel with a blocker is prepared in a procedure as described in our earlier work (Zheng et al, 2011). Specifically, for each atom in the biomolecule, van der Waals radius is assigned with the CHARMM22 force field (MacKerell Jr et al, 1998) and partial charge is obtained by the PDB2PQR software (Dolinsky et al, 2004, 2007). The molecular surface of the GA channel is generated by the MSMS program with density 10 and probe radius 1.4 Å (Sanner et al, 1996).

To demonstrate the blocker's gating behavior, we allow it to move along one direction just outside the channel mouth. The displacement of the blocker imitates the deflection of a hair bundle (Kennedy et al, 2005). The alteration in the blocker position changes the channel state. Additionally, to intensify the efficiency of the blocker, we allow its charge to be varied over a certain range in our numerical experiments.

The channel pore region is placed along the z -axis. The membrane part is added to the geometry from $z = 9$ Å to $z = 33$ Å (See Fig. 1). In order to find out the optimal position of the blocker, several locations along the channel axis (z -axis) were tested and then $z = -15.95$ Å is selected to be the most suitable z -coordinate. We fix the y -coordinate of the blocker at 0.1 Å and allow the blocker to move only along the x -direction from $x = -0.5$ Å to $x = 0.9$ Å, which involves the transition between the open and closed states of the channel.

2.2 The Poisson-Nernst-Planck (PNP) model

The PNP model (Chen and Eisenberg, 1993; Coalson and Kurnikova, 2005) is a relatively simple mathematical model, which is still able to incorporate the structural detail of the above prototype for the MET channel. It describes the dynamics and the transport of ion channels with relatively less computational cost. This model has been substantially discussed in the literature, including simplified Poisson-Boltzmann-Nernst-Planck model

(Zheng and Wei, 2011) and enriched variation multiscale models (Wei et al, 2012). A number of advanced mathematical techniques are used to solve the PNP equation with second order accuracy (Zheng et al, 2011).

2.2.1 Computational domain—Consider an open domain $\Omega = \Omega_m \cup \Omega_s \subset \mathbb{R}^3$, where Ω_m and Ω_s , respectively, denote the biomolecule region and solvent region (Zheng et al, 2011). In fact, Ω_m consists of channel protein and membrane layers, while Ω_s can be divided into bulk region and channel pore region as illustrated in Fig. 1. The interface between two regions Ω_m and Ω_s is represented by Γ , which is determined by the molecular surface.

2.2.2 Governing equations—The PNP model is a simplified continuum model which couples the Poisson equation and the Nernst-Planck equation (Zheng et al, 2011). The Poisson equation describes the electrostatic potential $\Phi(\mathbf{r})$ under the influence of dielectric properties, fixed charges in the protein and mobile charges in the solvent

$$-\nabla \cdot (\epsilon(\mathbf{r}) \nabla \Phi(\mathbf{r})) = 4\pi \left(\rho_f + \sum_{\beta=1}^{N_m} q_{\beta} C_{\beta}(\mathbf{r}) \right). \quad (1)$$

In Eq. (1), $\rho_f = \sum_{j=1}^{N_p} Q_j \delta(\mathbf{r} - \mathbf{r}_j)$ represents the fixed charges in the protein, where Q_j is the partial charge at position \mathbf{r}_j of the protein and N_p is the number of charged atoms in the protein. Moreover, partial charges in the membrane layers are neglected as a good approximation for ion transport. For each β , q_{β} and C_{β} are, respectively, the charge and concentration of β th ionic species and N_m represents the number of mobile ionic species in the solvent.

The space-dependent dielectric function $\epsilon(\mathbf{r})$ is defined as $\epsilon(\mathbf{r}) = \begin{cases} \epsilon_m, & \mathbf{r} \in \Omega_m \\ \epsilon_s, & \mathbf{r} \in \Omega_s \end{cases}$. In our computation, we set $\epsilon_m = 2$ for the molecular region impermeable to water or ions and $\epsilon_s = 80$ for the solvent region permeable to water and simple ions.

For each ionic species β in the solvent, the Nernst-Planck equation determines the rate of change of its concentration C_{β} by the Fick's law

$$\frac{\partial C_{\beta}(\mathbf{r})}{\partial t} = -\nabla \cdot \mathbf{J}_{\beta}(\mathbf{r}), \quad (2)$$

where \mathbf{J}_{β} is the concentration flux. Especially, the flux \mathbf{J}_{β} depends on the diffusion caused by the concentration gradient as well as the drift driven by the electrostatic potential gradient

$$\mathbf{J}_{\beta}(\mathbf{r}) = -D_{\beta}(\mathbf{r}) \left[\nabla C_{\beta}(\mathbf{r}) + \frac{q_{\beta}}{\kappa_B T} C_{\beta}(\mathbf{r}) \nabla \Phi(\mathbf{r}) \right], \quad (3)$$

where $D_{\beta}(\mathbf{r})$ is a diffusion coefficient of species β , κ_B is the Boltzmann constant and T is the absolute temperature.

The diffusion coefficient function $D_{\beta}(\mathbf{r})$ is defined to be a differentiable function as discussed in our earlier work (Zheng et al, 2011).

$$D_{\beta}(\mathbf{r}) = \begin{cases} D_{\beta,c}, & \mathbf{r} \in \Omega_{s,c} \\ D_{\beta,c} + (D_{\beta,c} - D_{\beta,b})f(\mathbf{r}), & \mathbf{r} \in \Omega_{s,u} \\ D_{\beta,b}, & \mathbf{r} \in \Omega_{s,b}, \end{cases}$$

where $\Omega_{s,c}$ is the channel region, $\Omega_{s,b}$ is the bulk region and $\Omega_{s,u}$ is a buffering zone between $\Omega_{s,c}$ and $\Omega_{s,b}$. The buffering zone is necessary to make the function $D(\mathbf{r})$ smooth. Here, we define

$$f(\mathbf{r}) = f(z) = \left\{ n \left(\frac{z - z_c}{z_b - z_c} \right)^{n+1} - (n+1) \left(\frac{z - z_c}{z_b - z_c} \right)^n \right\}$$

for $z \in [z_c, z_b]$, where z_c and z_b indicate the channel region and bulk region, respectively. The diffusion coefficients in the bulk region are determined as $D_{K^+,b} = 1.96 \times 10^{-5} \text{ cm}^2/\text{s}$ and $D_{Cl^-,b} = 2.03 \times 10^{-5} \text{ cm}^2/\text{s}$. For each species β , diffusion coefficient in the channel pore region is set to $D_{\beta,c} = D_{\beta,b}/21$ (Zheng et al, 2011).

The steady-state form of the Nernst-Planck equation is

$$\nabla \cdot D_{\beta}(\mathbf{r}) \left[\nabla C_{\beta}(\mathbf{r}) + \frac{q_{\beta}}{\kappa_B T} C_{\beta}(\mathbf{r}) \nabla \Phi(\mathbf{r}) \right] = 0 \text{ in } \Omega_s \quad (4)$$

with the zero-flux boundary condition

$$-D_{\beta}(\mathbf{r}) \left[\nabla C_{\beta}(\mathbf{r}) + \frac{q_{\beta}}{\kappa_B T} C_{\beta}(\mathbf{r}) \nabla \Phi(\mathbf{r}) \right] = 0 \text{ on } \Gamma,$$

which comes from the physical fact that no ion can penetrate through the interface. On the boundary Γ , we set $C(\mathbf{r}) = C_{\beta,0}$ as their bulk ion concentrations.

2.3 Computational algorithm

This section describes the computational method. The Dirichlet to Neumann mapping technique is used to remove charge singularities (Geng et al, 2007). In the MIB method, the standard centered finite difference scheme is implemented to handle regular points which are away from the interface and boundary, whereas irregular points which are close to the interface need some special manipulations to preserve the second order convergence of the numerical algorithm. A numerical overview of a second-order PNP solver (Zheng et al, 2011) and major principles of the matched interface and boundary (MIB) method are discussed. Coupled equations (4), (5) and (6) of the PNP model are solved iteratively.

2.3.1 Dirichlet to Neumann mapping—To avoid directly computing charge singularities due to the delta functions of ρ_f in the Poisson equation (1), $\Phi(\mathbf{r})$ is decomposed into the regular part $\bar{\Phi}(\mathbf{r})$ and the singular part $\Phi^s(\mathbf{r})$. Explicitly, the singular part $\Phi^s(\mathbf{r})$ is defined as (Geng et al, 2007)

$$\bar{\Phi}(\mathbf{r}) = \begin{cases} \Phi^s(\mathbf{r}) + \Phi^0(\mathbf{r}), & \mathbf{r} \in \Omega_m \\ 0, & \mathbf{r} \in \Omega_s, \end{cases}$$

where $\Phi^*(\mathbf{r})$ is the Green's function given by

$$\Phi^*(\mathbf{r}) = \sum_{j=1}^{N_p} \frac{q_j}{\varepsilon_m |\mathbf{r} - \mathbf{r}_j|}$$

and $\Phi^0(\mathbf{r})$ is the solution of the Laplace equation with a Dirichlet boundary condition

$$\begin{cases} \nabla^2 \Phi^0(\mathbf{r}) = 0, & \mathbf{r} \in \Omega_m \\ \Phi^0(\mathbf{r}) = -\Phi^*(\mathbf{r}), & \mathbf{r} \in \Gamma. \end{cases} \quad (5)$$

Then the Poisson equation of $\Phi(\mathbf{r})$ is obtained as follows

$$-\nabla \cdot (\varepsilon(\mathbf{r}) \nabla \Phi(\mathbf{r})) = 4\pi \sum_{\beta=1}^{N_m} q_\beta C_\beta(\mathbf{r}) \quad (6)$$

with two jump conditions at the interface

$$\begin{cases} [\Phi(\mathbf{r})] = 0, & \mathbf{r} \in \Gamma \\ [\varepsilon(\mathbf{r}) \nabla \Phi(\mathbf{r})] = \varepsilon_m \nabla (\Phi^*(\mathbf{r}) + \Phi^0(\mathbf{r})) \cdot \mathbf{n}, & \mathbf{r} \in \Gamma, \end{cases}$$

where \mathbf{n} is the outward normal direction of the interface.

2.3.2 Matched interface and boundary (MIB) method—The MIB method has been developed in our group in the past decade (Zhao and Wei, 2004; Zhou et al, 2006; Yu and Wei, 2007; Zheng et al, 2011). It is a higher-order numerical scheme for solving elliptic equations with discontinuous coefficients and complex interfaces and involving geometrical singularities. This scheme is based on the collocation scheme with Lagrange polynomials and it uses fictitious values and auxiliary points to enforce jump conditions at the interface. Additionally, this method transforms 3D problems into 1D-like ones. In this section, we discuss how to solve Eq. (6) for $\Phi(\mathbf{r})$ using the MIB method.

In Fig. 2, (x_i, y_j, z_k) is an irregular point. In fact, unlike the points (x_{i-1}, y_j, z_k) and (x_i, y_j, z_k) , only the point (x_{i+1}, y_j, z_k) belongs to Ω_m . Consequently, the discretization scheme along the x -direction at the point (x_i, y_j, z_k) involves the function values from different subdomains. Similarly, (x_{i+1}, y_j, z_k) is also an irregular point. For instance, the discretization schemes along the x -direction at these two irregular points, respectively, are

$$(\varepsilon \tilde{\Phi}_x)_x = \frac{\varepsilon_{i-\frac{1}{2}} \tilde{\Phi}_{i-1} - (\varepsilon_{i-\frac{1}{2}} + \varepsilon_{i+\frac{1}{2}}) \tilde{\Phi}_i + \varepsilon_{i+\frac{1}{2}} f_{i+1}}{\Delta x^2}$$

at (x_i, y_j, z_k) and

$$(\varepsilon \tilde{\Phi}_x)_x = \frac{\varepsilon_{i+\frac{1}{2}} f_i - (\varepsilon_{i+\frac{1}{2}} + \varepsilon_{i+\frac{3}{2}}) \tilde{\Phi}_{i+1} + \varepsilon_{i+\frac{3}{2}} \tilde{\Phi}_{i+2}}{\Delta x^2}$$

at (x_{i+1}, y_j, z_k) , where f_l denote the values at (x_l, y_j, z_k) .

The fictitious values $f_{i,j,k}$ and $f_{i+1,j,k}$ are determined by dealing with the continuity conditions [] and [\mathbf{n}]. First of all, a local coordinate transformation from (x, y, z) to (ξ, η, ζ) is applied to the point of intersection between the interface and the mesh line, where ξ is the normal direction, η is the tangential direction and ζ is the binormal direction. This new coordinates give rise to the following three jump conditions

$$\begin{bmatrix} [\varepsilon \tilde{\Phi}_\xi] \\ [\tilde{\Phi}_\eta] \\ [\tilde{\Phi}_\zeta] \end{bmatrix} = T \cdot \left(\begin{bmatrix} \varepsilon_m \tilde{\Phi}_x^m \\ \tilde{\Phi}_y^m \\ \tilde{\Phi}_z^m \end{bmatrix} - \begin{bmatrix} \varepsilon_s \tilde{\Phi}_x^s \\ \tilde{\Phi}_y^s \\ \tilde{\Phi}_z^s \end{bmatrix} \right). \quad (7)$$

Here the coordinate transformation matrix is

$$T = \begin{bmatrix} \sin\varphi\cos\theta & \sin\varphi\sin\theta & \cos\varphi \\ -\sin\theta & \cos\theta & 0 \\ -\cos\varphi\cos\theta & -\cos\varphi\sin\theta & \sin\varphi \end{bmatrix},$$

where φ and θ are the azimuth and zenith angles for the normal direction $\mathbf{n} = (\sin\varphi\cos\theta, \sin\varphi\sin\theta, \cos\varphi)$. The two jump conditions [], [] are obtained by differentiating [] along the tangential and binormal direction, respectively.

The jump conditions in Eq. (7) involve six partial derivatives $\tilde{\Phi}_x^m, \tilde{\Phi}_y^m, \tilde{\Phi}_z^m, \tilde{\Phi}_x^s, \tilde{\Phi}_y^s, \tilde{\Phi}_z^s$. Since two of them can be eliminated by using jump conditions, we select those partial derivatives that are relatively difficult to discretize to be eliminated. In an example of Fig 2, $\tilde{\Phi}_x^m$ and $\tilde{\Phi}_x^s$ are retained because the fictitious values are laid on the x -mesh line. Moreover, the geometrical complexity around point (x_o, y_j, z_k) , which is an intersecting point between the interface and the x -mesh line, may determine the selection strategy of the elimination of the partial derivatives. Appropriate values of a_1, a_2 and a_3 give

$$a_1[\varepsilon \tilde{\Phi}_\xi] + a_2[\tilde{\Phi}_\eta] + a_3[\tilde{\Phi}_\zeta] = c_1 \tilde{\Phi}_x^m + c_2 \tilde{\Phi}_x^s + c_3 \tilde{\Phi}_y^s + c_4 \tilde{\Phi}_z^s.$$

Auxiliary points are determined to evaluate $\tilde{\Phi}_y^s$ and $\tilde{\Phi}_z^s$. The modified jump conditions [] and $a_1[\] + a_2[\] + a_3[\]$ are solved to find the fictitious values $f_{i,j,k}$ and $f_{i+1,j,k}$. The more detailed equations are discussed in references (Yu and Wei, 2007).

2.3.3 Strategy of the second-order PNP solver—Eq. (5) is solved only once at the beginning because it does not involve concentrations of ionic species. The standard centered finite difference scheme is implemented to find $\phi^0(\mathbf{r})$ away from the complex boundary, while careful interpolation is required near the boundary (Yu and Wei, 2007). Moreover, for irregular points, the function values belong to Ω_s are replaced by those of intersecting points between the interface and grid lines. Similarly, the standard centered finite difference scheme is used to find the solution of Eq. (4) away from the boundary or interface for each ionic species as well. For the points near the interface, the difference scheme depends on geometry (The reference (Zheng et al, 2011) contains complete equations). Then Eq. (6) is solved for $\psi(\mathbf{r})$ using the MIB method to handle jump conditions [] and [\mathbf{n}] and to maintain the second order. Finally, the successive over relaxation (SOR)-like iterations for $C(\mathbf{r})$ and $\psi(\mathbf{r})$ guarantee the convergence. The iteration is repeated until the given tolerances are satisfied.

3 Results

3.1 Experimental data

In this work, experimental data from the reference (Kennedy et al, 2005) are utilized to compare with the computational results. Experiments were conducted on outer hair cells of Sprague-Dawley rats. At first, the apical turn of the organ of Corti was excised from rats between 6 and 14 days postnatal and prepared as previously reported in the literature (Kennedy et al, 2003, 2005; Beurg et al, 2008, 2010). The separated apical turn was fixed in the experimental chamber and the motion of a glass pipette deffects hair bundles, which activates the MET channels. Currents and bundle motions were recorded at the beginning of the apical turn of the bundle and averages of 10 stimuli were given to obtain a standard error of ± 1 (Kennedy et al, 2005).

We mainly focus on the MET channel current. The graph of the MET channel current against time can be divided into three steps (Kennedy et al, 2005). The first step represents that the channels respond to the bundle motions within microseconds, which proves the direct relationship between bundle motion and channel activation. Then the second and third parts, respectively, describe fast and slow adaptations which indicate the channel closure and the restoration of the sensitivity of the hair bundle. Next, the normalized current (I/I_{Max}), which can be regarded as the channel open probability, is also presented in the reference (Kennedy et al, 2005). The relation between the normalized current and the displacement of the bundle shows a nonlinear sigmoidal behavior. It also demonstrates that the positive defection (toward the longest stereocilium) increases the open probability; on the contrary, the negative defection (away from the longest stereocilium) decreases the open probability.

3.2 Computational results

We explore the behavior of our MET prototype under various conditions. One of the basic issues is the electrostatic potential profile projected to the channel direction (z -direction) at the middle of the channel pore. Except specified, we set the charge of the blocker as $q = 2$, the bulk concentrations of both ions $C_0 = C_{\text{K}^+,0} = C_{\text{Cl}^-,0} = 0.1 \text{ M}$ and applied external voltage $V_0 = 100 \text{ mV}$. We first examine the impact of moving the charged blocker along the x -direction. The goal of this study is to verify whether the proposed MET prototype properly represents the behavior of the MET channel. We move the charged blocker from $x = -0.5 \text{ \AA}$ to 0.9 \AA . As illustrated in Fig. 3, at locations $x = 0.6 \text{ \AA}$ and $x = 0.9 \text{ \AA}$, the charged blocker creates a large electrostatic barrier at the channel mouth region, which hinders the inward flow of the cation K^+ . As a result, the electrostatic potential level inside the channel is very low due to the fact that the positive ions cannot effectively enter through the channel. Therefore, the proposed MET prototype shows a desirable gating effect.

We next examine the behavior of our model under different bulk concentrations. We still set $q = 2$ for the blocker charge and $V_0 = 100 \text{ mV}$ for the applied voltage. Two different bulk ion concentrations $C_0 = 0.1 \text{ M}$ and $C_0 = 0.2 \text{ M}$ are tested in our numerical experiments. In Fig. 4(a), we illustrate the response of the present model at these two bulk ion concentrations by showing the electrostatic potential curve along the channel pore direction. The change in the bulk ion concentration has little influence on the electrostatic profile outside of the channel pore region, which is dominated by the applied voltage and reflects the electrical neutralization of cations and anions. However, the increase in the bulk ion concentration leads to a higher concentration of the positive ion in the channel pore region, which enhances the electrostatic potential within the channel as well.

We further investigate the behavior of our model under two different applied voltages. To this end, we set $q = 2$ and $C_0 = 0.1 \text{ M}$. The applied voltage is changed from $V_0 = 100 \text{ mV}$ to

$\phi_0 = 200$ mV. The electrostatic potential in response to the change is depicted at Fig. 4(b). We see an obvious change in the electrostatic potential in the left bulk region and in the left part of the channel pore region.

To demonstrate the effectiveness of the charged blocker, we study the impact of the displacement of the blocker along the x -direction under the fixed blocker charge $q = 2$ as shown in Fig. 5. We also analyze the behavior under two bulk ion concentrations $C_0 = 0.1$ M and $C_0 = 0.2$ M as shown in Fig. 5(a) and two applied voltages $\phi_0 = 100$ mV and $\phi_0 = 200$ mV as shown in Fig. 5(b). We define a relative displacement d_x as the scaled distance of the blocker from its optimal position. When the relative displacement is zero, i.e., $d_x = 0$, the blocker locates right on top the channel mouth, which essentially blocks the channel and creates the closed state. When $d_x = 1$, there is no blocking effect and the system reaches its normal open state. Clearly, the current gets higher as the relative displacement increases. Meanwhile, the channel current increases as the bulk ion concentration increases, because of permeating more cations, which is consistent with the increase in the electrostatic potential within the channel pore region shown in Fig. 4(a). Similarly, the current increases as the applied external voltage increases, due to the increase in the electrostatic potential as shown in Fig. 4(b). These results agree qualitatively with those of hair bundle defections in the literature (Kennedy et al, 2003, 2005).

Having established the importance of the blocker position to the channel open-closed transition, we are interested in other properties of the blocker that may contribute to its gating mechanism. Two most relevant properties are the blocker size and charge. In the present system, the change of the molecular size of the blocker is ineffective to the behavior of the channel because the PNP model does not consider the finite volume effect (Jung et al, 2009; Lu and Zhou, 2011). However, it can be studied how the blocker charge affects the ion transport. To this end, we test our model with a number of different charges, namely, $q = 0.5$, $q = 1$, $q = 1.5$ and $q = 2$, while set $C_0 = 0.1$ M and $\phi_0 = 100$ mV. Our results are presented in Fig. 6. In Fig. 6 (a), the electrostatic potential at the entrance of the channel is dramatically influenced by the magnitude of the blocker charge. A larger charge leads to a higher potential barrier, which results in less density of the cation and a lower electrostatic potential within the channel pore region. In Fig. 6 (b), we illustrate the impact of the blocker charge to the channel current under various relative blocker displacement d_x . It is interesting to note that only when the charge reaches an appropriate threshold, the blocker can effectively close the channel. Therefore, a leakage ion current exists when the blocker does not carry sufficient charge or is not located at its optimized position.

It is interesting to compare our model prediction with the experimental finding of the relation between the open probability and the rat hair bundle displacement given in the reference (Kennedy et al, 2005). To this end, we compute the channel open probability P_o at a number of relative displacement d_x with four different charges when we set $C_0 = 0.1$ M and $\phi_0 = 100$ mV. For a comparison, our results are presented in Fig. 7 together with experimental data (Kennedy et al, 2005). Amazingly, there is an excellent agreement between our model prediction and experimental measurement when the blocker charge is $q = 2$, indicating that $q = 2$ is the optimal charge in our molecular level prototype of the MET channel. Furthermore, this result implies that our molecular level prototype is able to reveal the gating mechanism of the MET channel.

Finally, our optimal model predictions are obtained with fixed applied voltage and bulk ion concentration. Obviously, it remains to investigate whether our model prediction is sensitive to the change of these experimental conditions. As shown in Fig. 8, although bulk ion concentration and applied external voltage are doubled in our numerical simulations, our model prediction does not change very much. Additionally, there is still an excellent

consistency between our MET model prediction and experimental measurement (Kennedy et al, 2005). This result further validates the robustness of our molecular level prototype for the rat MET channel.

4 Conclusion

The auditory system is one of the most significant sensory systems for mammals. Mechano-electrical transducer (MET) is a principal device in mammalian auditory system for the brain to perceive sounds. It is generally speculated that hair cell deflections regulate the MET channels. However, the molecular building blocks of the MET channel are not yet available to date and its gating mechanism is still elusive. In this work, we present a molecular level prototype for the mammalian MET channel to elucidate the gating mechanism of mechanotransduction channel in mammals. Our MET prototype consists of a realistic ion channel, the Gramicidin A (GA) channel (PDB ID: 1MAG), an additional charged lip, called a blocker and positioned in the GA channel mouth region, and membrane layers.

To explore the physical properties of the proposed MET prototype, we employ a well tested theoretical model, the Poisson-Nernst-Planck (PNP) model, for three dimensional (3D) numerical simulation of the MET channel transport. Advanced computational techniques, such as Dirichlet-to-Neumann mapping (DNM) and matched interface and boundary (MIB) method developed in our earlier work are utilized for the present numerical simulations. We design an extensive numerical experiment to analyze in detail the electrostatic potential and channel current in response to variations of blocker charge, blocker relative displacement, bulk ion concentration and applied external voltage. Finally, we compare our prototype prediction of channel open probability versus relative displacement with that of experimental measurement from rat outer hair cells (Kennedy et al, 2005). Excellent consistency between our model prediction and experimental data is observed. We further demonstrate that our model prediction is insensitive to the change in bulk ion concentration and applied external voltage. Our findings indicate that hair-cell tip links, which connect hair bundles, efficiently convey mechanical force to mechanosensitive transduction channels and manage their opening and closing.

Acknowledgments

JP thanks Ms Qiong Zheng and Dr Kelin Xia for technical assistance. This work was supported in part by NSF grants CCF-0936830, DMS-1160352 and NIH grant R01GM-090208.

References

- Beurg M, Nam JH, Crawford A, Fettiplace R. The actions of calcium on hair bundle mechanics in mammalian cochlear hair cells. *Biophysical journal*. 2008; 94(7):2639–2653. [PubMed: 18178649]
- Beurg M, Fettiplace R, Nam JH, Ricci AJ. Localization of inner hair cell mechanotransducer channels using high-speed calcium imaging. *Nature neuroscience*. 2009; 12(5):553–558.
- Beurg M, Nam JH, Chen Q, Fettiplace R. Calcium balance and mechanotransduction in rat cochlear hair cells. *Journal of neurophysiology*. 2010; 104(1):18–34. [PubMed: 20427623]
- Borisjuk A. Physiology and mathematical modeling of the auditory system. *Tutorials in Mathematical Biosciences I*. 2005:107–168.
- Chen D, Eisenberg R. Charges, currents, and potentials in ionic channels of one conformation. *Biophysical Journal*. 1993; 64(5):1405–1421. [PubMed: 7686784]
- Chen D, Wei GW. Quantum dynamics in continuum for proton transport generalized correlation. *The Journal of Chemical Physics*. 2012; 136:134,109.
- Coalson RD, Kurnikova MG. Poisson-Nernst-Planck theory approach to the calculation of current through biological ion channels. *NanoBioscience, IEEE Transactions on*. 2005; 4(1):81–93.

- Denk W, Holt JR, Shepherd GMG, Corey DP. Calcium imaging of single stereocilia in hair cells: localization of transduction channels at both ends of tip links. *Neuron*. 1995; 15(6):1311–1321. [PubMed: 8845155]
- Dolinsky T, Nielsen J, McCammon J, Baker N. Pdb2pqr: an automated pipeline for the setup of poisson-boltzmann electrostatics calculations. *Nucleic acids research*. 2004; 32(suppl 2):W665–W667. [PubMed: 15215472]
- Dolinsky T, Czodrowski P, Li H, Nielsen J, Jensen J, Klebe G, Baker N. Pdb2pqr: expanding and upgrading automated preparation of biomolecular structures for molecular simulations. *Nucleic acids research*. 2007; 35(suppl 2):W522–W525. [PubMed: 17488841]
- Eisenberg BS, Hyon YK, Liu C. Energy variational analysis of ions in water and channels: Field theory for primitive models of complex ionic fluids. *Journal of Chemical Physics*. 2010; 133:104,104.
- Farris HE, LeBlanc CL, Goswami J, Ricci AJ. Probing the pore of the auditory hair cell mechanotransducer channel in turtle. *The Journal of physiology*. 2004; 558(3):769–792. [PubMed: 15181168]
- Fettiplace R. Defining features of the hair cell mechanoelectrical transducer channel. *Pflügers Archiv European Journal of Physiology*. 2009; 458(6):1115–1123. [PubMed: 19475417]
- Fettiplace R, Hackney CM. The sensory and motor roles of auditory hair cells. *Nature Reviews Neuroscience*. 2006; 7(1):19–29.
- Geng W, Yu S, Wei G. Treatment of charge singularities in implicit solvent models. *The Journal of chemical physics*. 2007; 127:114,106.
- Gillespie PG, Müller U. Mechanotransduction by hair cells: Models, molecules, and mechanisms. *Cell*. 2009; 139(1):33–44. [PubMed: 19804752]
- Hacker, MP.; Messer, WS.; Bachmann, KA. *Pharmacology: Principles and practice*. Academic Press; 2009.
- Hodgkin AL, Huxley AF. The dual effect of membrane potential on sodium conductance in the giant axon of *Loligo*. *The Journal of physiology*. 1952; 116(4):497–506. [PubMed: 14946715]
- Hollerbach U, Chen DP, Eisenberg RS. Two-and three-dimensional Poisson-Nernst-Planck simulations of current flow through gramicidin A. *Journal of Scientific Computing*. 2001; 16(4):373–409.
- Howard J, Hudspeth AJ. Compliance of the hair bundle associated with gating of mechanoelectrical transduction channels in the bullfrog's saccular hair cell. *Neuron*. 1988; 1(3):189–199. [PubMed: 2483095]
- Jaramillo F, Hudspeth AJ. Localization of the hair cell's transduction channels at the hair bundle's top by iontophoretic application of a channel blocker. *Neuron*. 1991; 7(3):409–420. [PubMed: 1716929]
- Jordan PC. Fifty years of progress in ion channel research. *NanoBioscience, IEEE Transactions on*. 2005; 4(1):3–9.
- Jung YW, Lu B, Mascagni M. A computational study of ion conductance in the kcsa k channel using a nernst-planck model with explicit resident ions. *The Journal of chemical physics*. 2009; 131:215,101.
- Kazmierczak P, Müller U. Sensing sound: molecules that orchestrate mechanotransduction by hair cells. *Trends in Neurosciences*. 2012; 35(4):220–229. [PubMed: 22177415]
- Kazmierczak P, Sakaguchi H, Tokita J, Wilson-Kubalek EM, Milligan RA, Müller U, Kachar B. Cadherin tip-link filaments in sensory hair cells. *Nature*. 2007; 449(7158):87–91. [PubMed: 17805295]
- Kennedy HJ, Evans MG, Crawford AC, Fettiplace R. Fast adaptation of mechanoelectrical transducer channels in mammalian cochlear hair cells. *Nature neuroscience*. 2003; 6(8):832–836.
- Kennedy HJ, Crawford AC, Fettiplace R. Force generation by mammalian hair bundles supports a role in cochlear amplification. *Nature*. 2005; 433(7028):880–883. [PubMed: 15696193]
- Lu B, Zhou Y. Poisson-nernst-planck equations for simulating biomolecular diffusion-reaction processes ii: Size effects on ionic distributions and diffusion-reaction rates. *Biophysical Journal*. 2011; 100(10):2475–2485. [PubMed: 21575582]

- Lu B, Zhou Y, Huber G, Bond S, Holst M, McCammon J. Electrodiffusion: A continuum modeling framework for biomolecular systems with realistic spatiotemporal resolution. *The Journal of chemical physics*. 2007; 127:135,102.
- MacKerell A Jr, Bashford D, Bellott M, Dunbrack R Jr, Evanseck J, Field M, Fischer S, Gao J, Guo H, Ha S, et al. All-atom empirical potential for molecular modeling and dynamics studies of proteins. *The Journal of Physical Chemistry B*. 1998; 102(18):3586–3616.
- Peng AW, Salles FT, Pan B, Ricci AJ. Integrating the biophysical and molecular mechanisms of auditory hair cell mechanotransduction. *Nature Communications*. 2011; 2:523.
- Ricci AJ, Crawford AC, Fettiplace R. Tonotopic variation in the conductance of the hair cell mechanotransducer channel. *Neuron*. 2003; 40(5):983–990. [PubMed: 14659096]
- Ricci AJ, Kachar B, Gale J, Van Netten SM. Mechano-electrical transduction: new insights into old ideas. *Journal of Membrane Biology*. 2006; 209(2):71–88. [PubMed: 16773495]
- Roux B, Allen T, Berneche S, Im W. Theoretical and computational models of biological ion channels. *Quarterly reviews of biophysics*. 2004; 37(01):15–103. [PubMed: 17390604]
- Sanner M, Olson A, Spohner J. Reduced surface: an efficient way to compute molecular surfaces. *Biopolymers*. 1996; 38(3):305–320. [PubMed: 8906967]
- Schwander M, Kachar B, Müller U. Review series: The cell biology of hearing. *The Journal of cell biology*. 2010; 190(1):9–20. [PubMed: 20624897]
- Wei GW, Zheng Q, Chen Z, Xia K. Variational multiscale models for charge transport. *SIAM Review*. 2012; 54(4):699–754. [PubMed: 23172978]
- Yu SN, Wei GW. Three-dimensional matched interface and boundary (MIB) method for treating geometric singularities. *Journal of Computational Physics*. 2007; 227(1):602–632.
- Zhao S, Wei GW. High-order FDTD methods via derivative matching for Maxwell's equations with material interfaces. *Journal of Computational Physics*. 2004; 200(1):60–103.
- Zheng Q, Wei GW. Poisson-Boltzmann-Nernst-Planck model. *The Journal of chemical physics*. 2011; 134:194,101.
- Zheng Q, Chen D, Wei GW. Second-order Poisson Nernst-Planck solver for ion transport. *Journal of computational physics*. 2011; 230:5239–5262. [PubMed: 21552336]
- Zhou YC, Zhao S, Feig M, Wei GW. High order matched interface and boundary method for elliptic equations with discontinuous coefficients and singular sources. *Journal of Computational Physics*. 2006; 213(1):1–30.

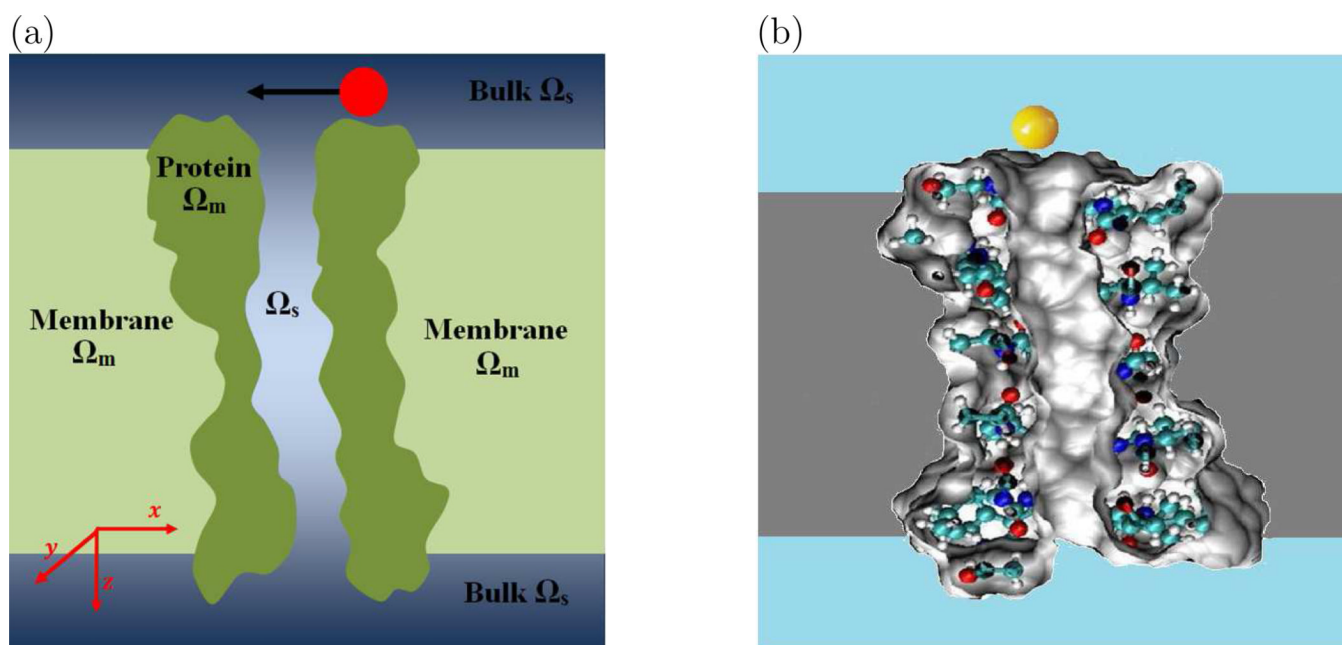


Fig. 1.
An illustration of the model setup and the computational domain. (a) The domain is composed of four regions: protein region, membrane layers, bulk region and channel pore region. The sphere represents the blocker and the arrow indicates the direction of its movement. (b) The GA channel protein, the artificial membrane, and the blocker.

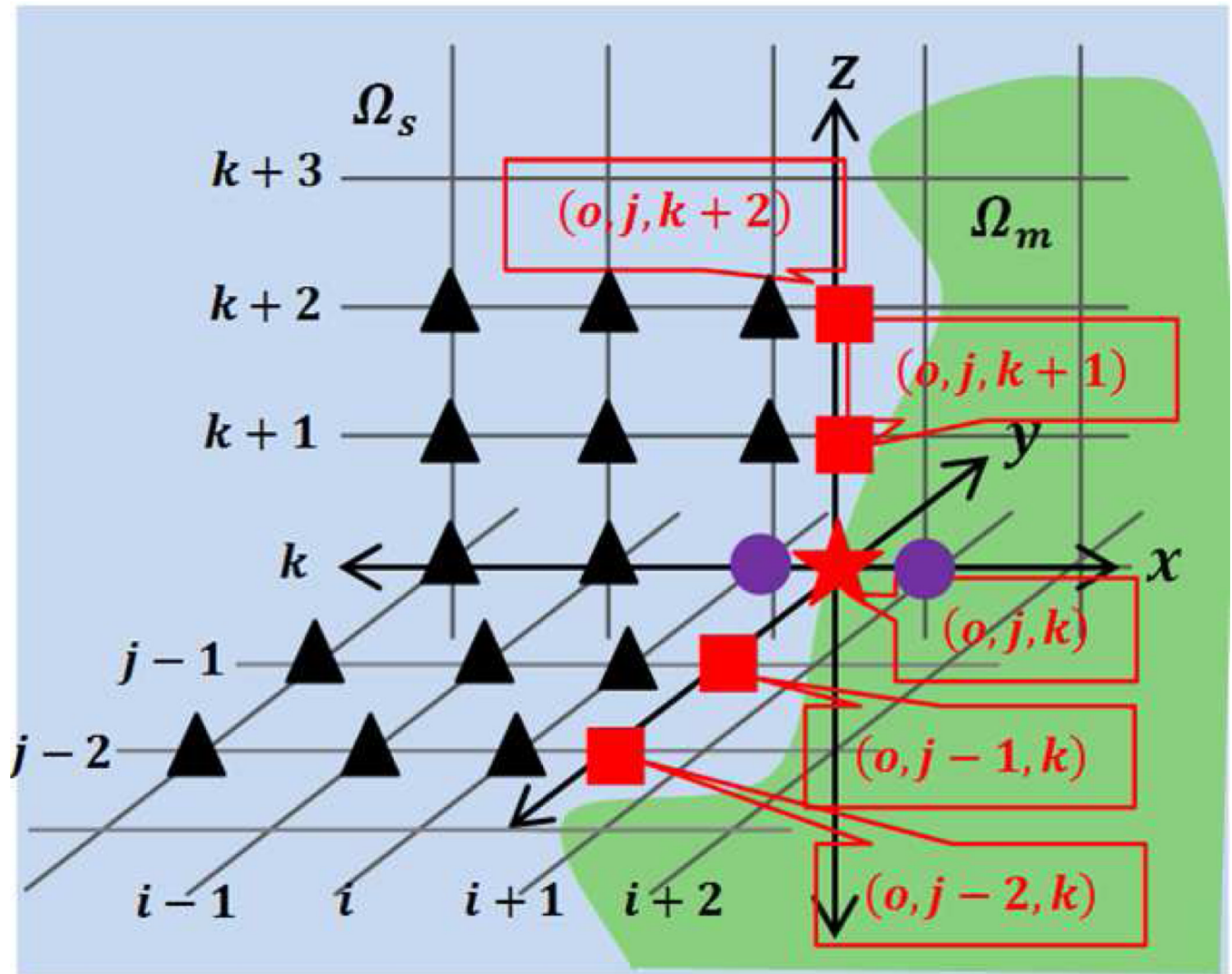


Fig. 2.

An illustration of the interface. The k th mesh line intersects the interface at the point (x_o, y_j, z_k) (star). Two irregular points (circle) (x_i, y_j, z_k) and (x_{i+1}, y_j, z_k) give two fictitious values $f_{i,j,k}$ and $f_{i+1,j,k}$. Two auxiliary points (square) on the y -direction are (x_o, y_{j-2}, z_k) and (x_o, y_{j-1}, z_k) and two auxiliary points (square) on the z -direction are (x_o, y_j, z_{k+1}) and (x_o, y_j, z_{k+2}) . Triangles indicate the chosen points to interpolate at the auxiliary points.

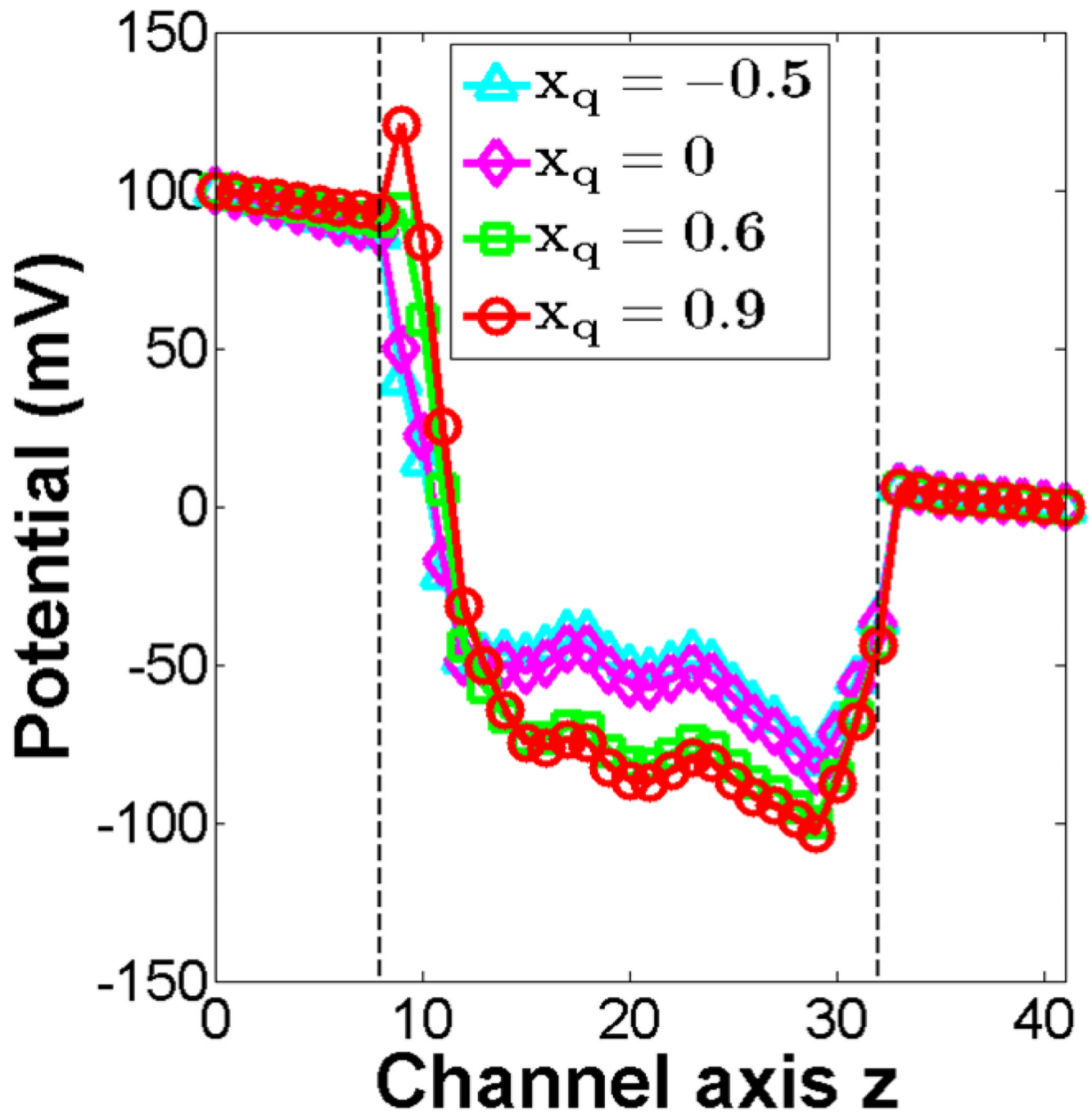
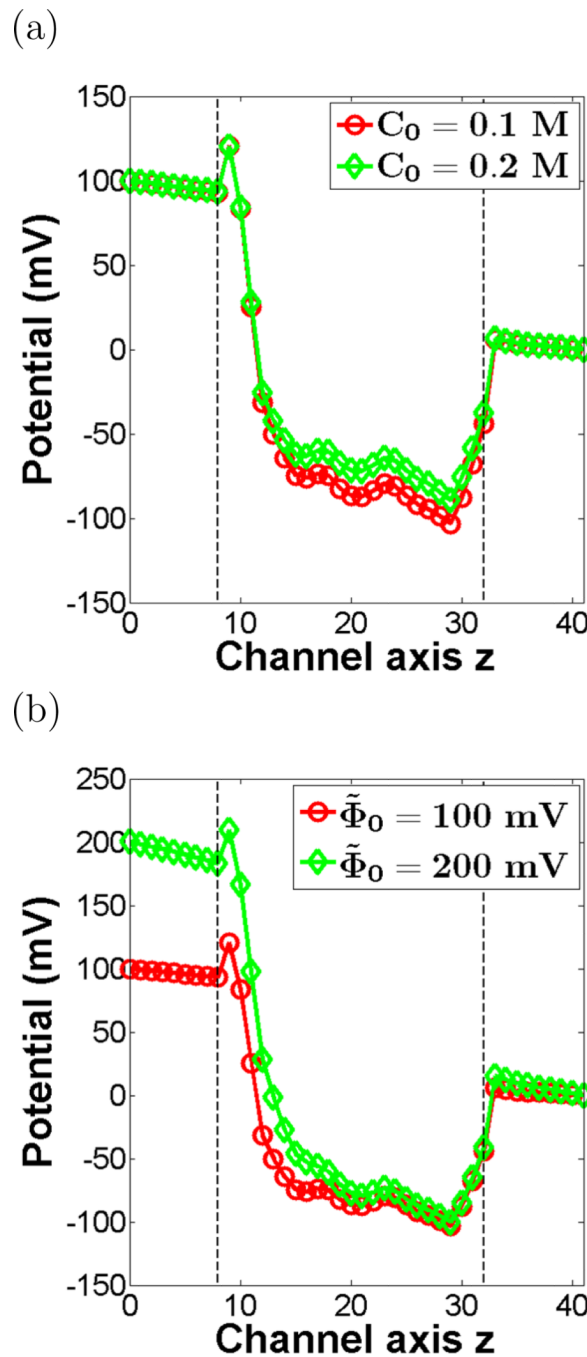
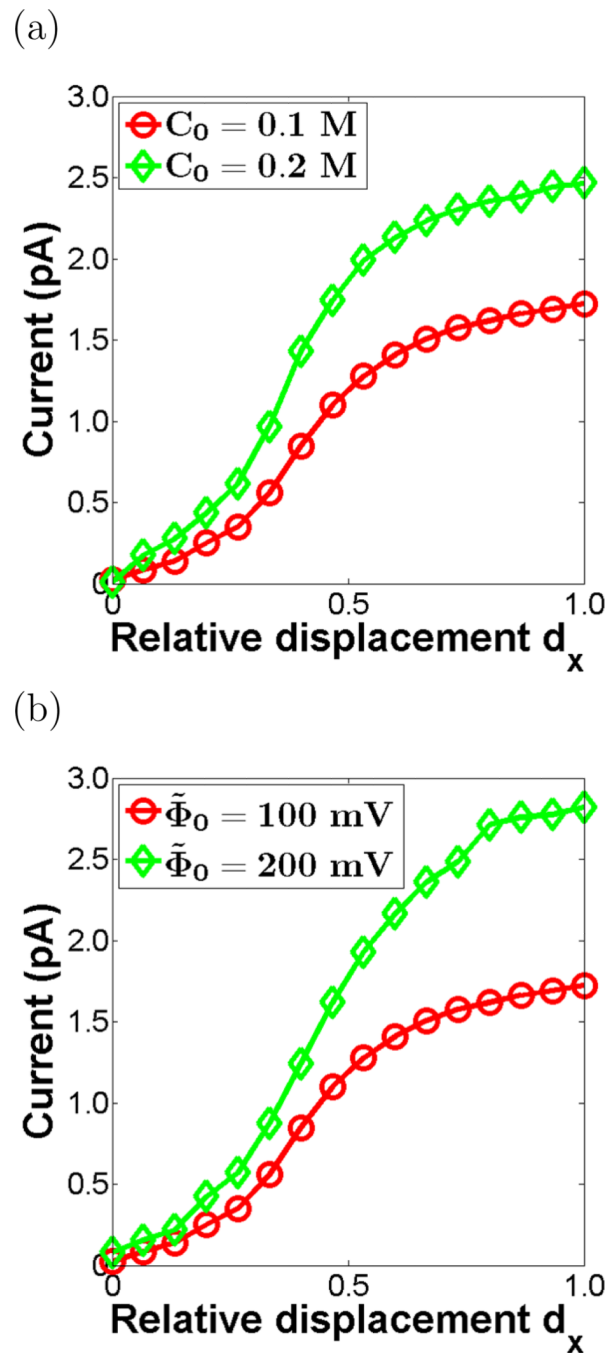


Fig. 3.

Electrostatic potential profiles at different locations x_q of the blocker with charge $q = 2$, $C_0 = C_{K^+,0} = C_{Cl^-,0} = 0.1$ M and $\phi_0 = 100$ mV. The region between two dashed lines indicates the channel pore region. As the blocker position gets closer to 0.9, the blocker produces a stronger barrier near the mouth of the channel as shown in the electrostatic potential profile.

**Fig. 4.**

Electrostatic potential profiles along the channel direction for the MET prototype. The region between two dashed lines indicates the channel pore region. (a) Effect of different bulk ion concentrations $C_0 = C_{K^+,0} = C_{Cl^-,0} = 0.1$ M (circles) and $C_0 = C_{K^+,0} = C_{Cl^-,0} = 0.2$ M (diamonds) when $q = 2$ and $\Phi_0 = 100$ mV are fixed; (b) Effect of different applied external voltages $\Phi_0 = 100$ mV (circles) and $\Phi_0 = 200$ mV (diamonds) when $q = 2$ and $C_0 = 0.1$ M are fixed. Increase in the bulk ion concentration creates higher potential within the channel. Similarly, the increase in the applied external voltage leads to high electrostatic potential in the left bulk region as well as in the channel pore region.

**Fig. 5.**

The channel current versus the relative displacement (d_x) of the charged blocker. (a) Behavior under two bulk ion concentrations $C_0 = C_{K^+,0} = C_{Cl^-,0} = 0.1 \text{ M}$ (circles) and $C_0 = C_{K^+,0} = C_{Cl^-,0} = 0.2 \text{ M}$ (diamonds) when $q = 2$ and $\tilde{\Phi}_0 = 100 \text{ mV}$ are fixed; (b) external voltages $\tilde{\Phi}_0 = 100 \text{ mV}$ (circles) and $\tilde{\Phi}_0 = 200 \text{ mV}$ (diamonds) when $q = 2$ and $C_0 = 0.1 \text{ M}$ are fixed. Consequently, increase in bulk ion concentration and in external voltage induces increase in channel current.

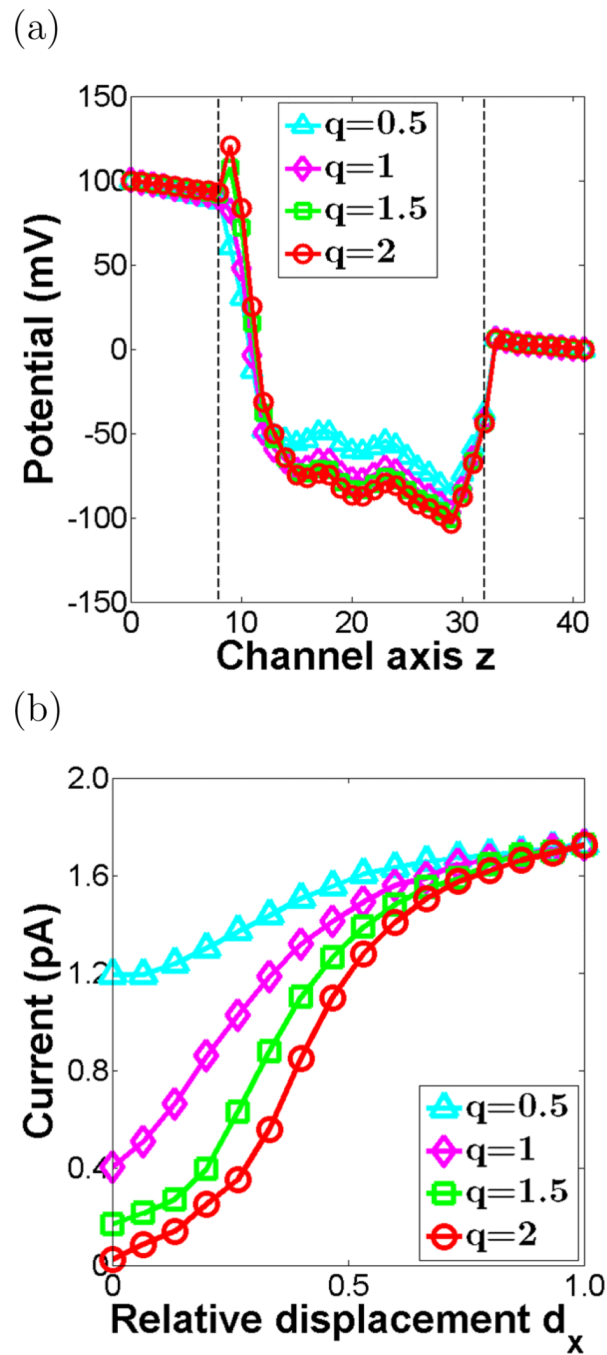


Fig. 6.

(a) Electrostatic potential profiles and (b) channel current values for four different charges $q = 0.5$, $q = 1$, $q = 1.5$ and $q = 2$ when $C_0 = 0.1$ M and $\phi_0 = 100$ mV are fixed. The region between two dashed lines indicates the channel pore region. As the charge gets increased, the barrier at the gate of the channel gets higher. In conclusion, the amplitude of the current curve also gets enlarged.

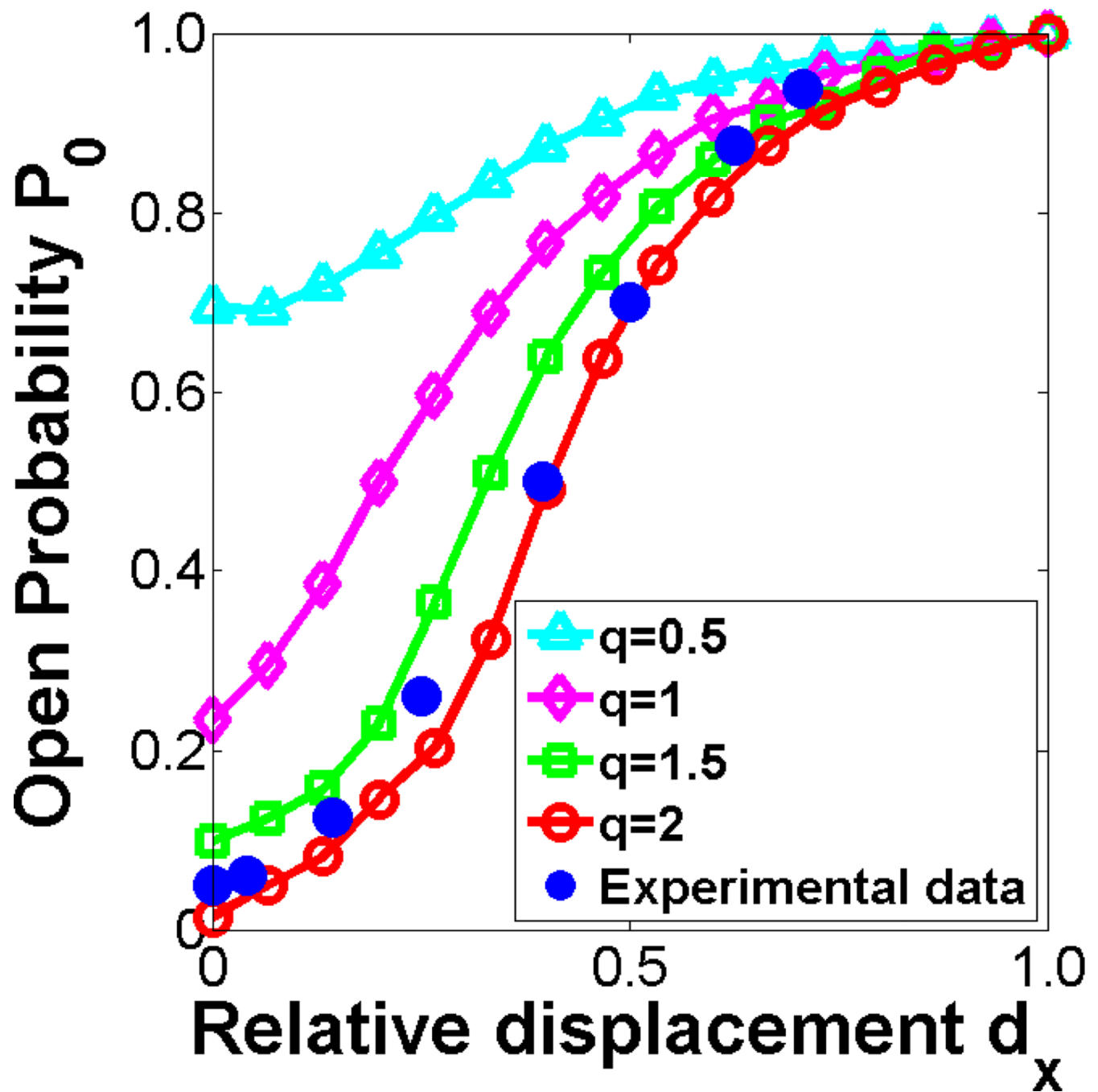


Fig. 7.

Open probability P_0 is plotted against the relative displacement d_x for four different charges $q = 0.5$, $q = 1$, $q = 1.5$ and $q = 2$ when $C_0 = 0.1$ M and $\phi_0 = 100$ mV. The solid dots are experimental data of the normalized MET current versus normalized rat hair bundle displacement (Kennedy et al, 2005). At each blocker charge, the open probability in response to the relative displacement forms a sigmoidal shape and, especially, the charge $q = 2$ gives a remarkable agreement with the experimental data.

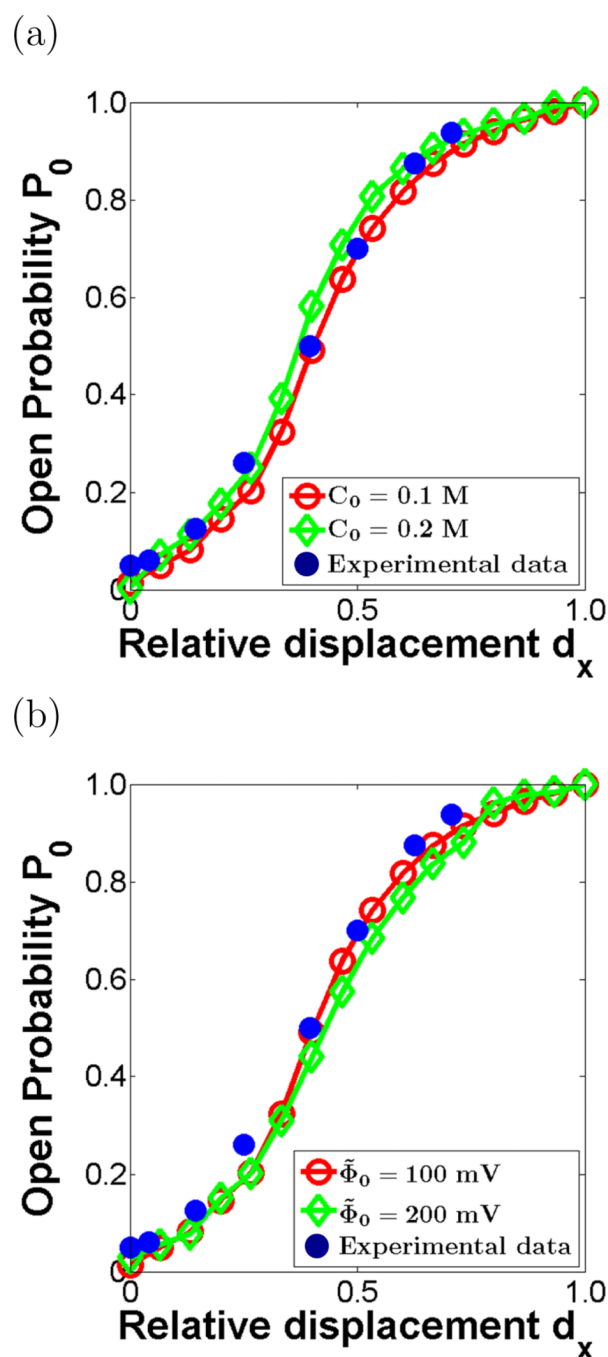


Fig. 8. Sensitivity test of the molecular level MET model for the prediction of open-closed probability according to the relative displacement of the blocker. (a) The bulk ion concentration is doubled; (b) The applied external voltage is doubled. Both cases are fairly consistent with the experimental finding (Kennedy et al, 2005).